

The effect of the initial microstructure in terms of sink strength on the ion-irradiation-induced hardening of ODS alloys studied by nanoindentation¹

Binghuang Duan^{a,b}, Cornelia Heintze^b, Frank Bergner^{b,*}, Andreas Ulbricht^b, Shavkat Akhmadaliev^b, Elvira Oñorbe^c, Yann de Carlan^d, Tieshan Wang^a

^a School of Nuclear Science and Technology, Lanzhou University, Lanzhou 730000, PR China

^b Helmholtz-Zentrum Dresden-Rossendorf, Bautzner Landstraße 400, 01328 Dresden, Germany

^c CIEMAT, Division of Structural Materials, Avenida Complutense, 40, 28040 Madrid, Spain

^d CEA/DEN/DMN/SRMA, CEA Saclay, 91191 Gif-sur-Yvette Cedex, France

Key words: Oxide dispersion strengthened alloys; Ion irradiation; Nanoindentation; hardening; Sink strength.

Abstract

Oxide dispersion strengthened (ODS) Fe-Cr alloys are promising candidates for structural components in nuclear energy production. The small grain size, high dislocation density and the presence of particle matrix interfaces may contribute to the improved irradiation resistance of this class of alloys by providing sinks and/or traps for irradiation-induced point defects. The extent to which these effects impede hardening is still a matter of debate. To address this problem, a set of alloys of different grain size, dislocation density and oxide particle distribution were selected. In this study, three-step Fe-ion irradiation at both 300 °C and 500 °C up to 10 dpa was used to introduce damage in five different materials including three 9Cr-ODS alloys, one 14Cr-ODS alloy and one 14Cr-non-ODS alloy. Electron backscatter diffraction (EBSD), transmission electron microscopy (TEM), small angle neutron scattering (SANS), and nanoindentation testing were applied, the latter before and after irradiation. Significant hardening occurred for all materials and temperatures, but it is distinctly lower in the 14Cr alloys and also tends to be lower at the higher temperature. The possible contribution of Cr-rich α' -phase particles is addressed. The impact of grain size, dislocation density and particle distribution is demonstrated in terms of an empirical trend between total sink strength and hardening.

1. Introduction

Oxide dispersion strengthened (ODS) alloys are promising candidates for structural materials of future Generation IV fission reactors and fusion devices [1-4]. Compared with conventional ferritic/martensitic alloys they show superior performance when exposed to large dose of neutron irradiation and high operating temperatures [4, 5].

The introduction of oxide nanoparticles gives rise to a high density of particle-matrix interfaces, small grain sizes and a high dislocation density. These microstructural features contribute to the initial hardness of the material and may act as sinks for irradiation-induced

¹ Published as: B. Duan et al., J. Nucl. Mater. 495 (2017) 118-127

* Corresponding author. E-mail address: f.bergner@hzdr.de (F. Bergner).

point defects. Here we are interested in the latter aspect. The extent to which particle-matrix interfaces, grain boundaries and dislocations act as sinks and, therefore, impede irradiation hardening is still a matter of debate [6-8]. The concept of sink strength is well established within a theoretical framework based on rate theory [9]. However, there are few experimental studies [4, 10-12] quantitatively relating the reduction of irradiation-induced hardening to the existing sinks in ODS alloys.

Zinkle and Snead [4] summarized the effect of the initial sink strength on neutron irradiation-induced hardening of several ferritic/martensitic steels including ODS steels. They reported little effect of the total sink strength on irradiation hardening for sink strengths less than approximately 10^{16} m^{-2} , but a clear trend for reduced irradiation hardening beyond 10^{16} m^{-2} .

To further substantiate the correlation between the irradiation-induced hardening and the sink strength arising from particle-matrix interfaces, grain boundaries and dislocations, five alloys with various oxide nanoparticle distributions, grain size distributions, and dislocation densities were irradiated with Fe ions up to 10 dpa at 300 °C and 500 °C. Three of the ODS alloys, namely ODS Fe-9Cr (wt%) in the as-received (ferritic) condition, the same alloy in the quenched and tempered condition, and a ferritic ODS Fe-14Cr alloy, were distributed within the European collaborative project MatISSE (see acknowledgement). Samples of ODS Eurofer and an Fe-14Cr alloy, the latter produced via the powder metallurgy route but without addition of yttria powder, are included in the study in order to extend the range of variation of the microstructures and to strengthen the conclusions. The irradiation-induced hardness increase was measured using nanoindentation. The sink strengths were derived from the microstructural observations based on the application of electron backscatter diffraction (EBSD) to measure average grain size and small-angle neutron scattering (SANS) to measure the size distribution and number density of the oxide nanoparticles. Dislocation densities were measured by transmission electron microscopy (TEM) or adopted from the literature, if available. The calculation of sink strength was based on published expressions [9].

The materials, ion irradiations and experimental methods are introduced in section 2. Sections 3 and 4 are dedicated to the experimental results and the discussion, respectively. Three aspects are considered in the discussion: the indentation hardness of the unirradiated materials, the effect of the irradiation temperature (300 °C versus 500 °C) and the impact of the microstructure on irradiation hardening in terms of sink strength.

2. Experiments

2.1 Materials and samples

Four ODS alloys and one alloy without the addition of Y_2O_3 particles were investigated. The chemical composition information is summarized in Table 1.

An Fe-14Cr alloy without the addition of Y_2O_3 powder (labelled 14Cr-non-ODS in this study) was prepared by CEA, France, from gas-atomized pre-powder [13]. The milled powder was encapsulated, degassed in vacuum and then pre-sintered at 1100 °C for 1 hour. Finally hot extrusion at 1100 °C with a speed of 25 mm/s and an extrusion ratio of 13 was performed.

A corresponding Fe-14Cr alloy with the addition of 0.3 wt.% Y_2O_3 powder (code J27-M2, here labelled 14Cr-ODS) was supplied by CEA, France. It was prepared from the master alloy in a vertical attritor under hydrogen atmosphere protection, followed by hot extrusion at 1000 °C and annealing for 1.5 h at 1050 °C. See [14] for more details about this material and research results.

An Fe-9Cr alloy with the addition of 0.3 wt.% Y_2O_3 powder (code L22-M1) was also supplied by CEA, France. Gas-atomized powder was milled in a vertical attritor under hydrogen atmosphere protection. Afterwards, encapsulation, degassing, hot extrusion and air cooling were performed to produce extruded bars. Part of this material (labelled 9Cr-ODS-A) was investigated in the as-received (ferritic) condition. Another part of the same material (labelled 9Cr-ODS-B) was additionally exposed to a heat treatment consisting of austenitization at 1050 °C for 0.5 h, quenching in oil at a cooling rate higher than 10 K/s and tempering at 750 °C for 1 h. The heat treatment was conducted to achieve finer grain size distribution and martensite.

ODS-Eurofer was provided by KIT, Germany, and fabricated from gas-atomized Eurofer97 with 0.3 wt.% Y_2O_3 powder. Hot isostatic pressing (HIP) was chosen for consolidation, followed by hot rolling to 6 mm thick plates. The plates were subsequently austenitized at 1100 °C for 0.5 h, followed by water quenching and tempering at 750 °C for 2 h. Considering that substantial investigations have been accomplished on ODS-Eurofer, here it was selected and employed mainly as a reference 9Cr-ODS alloy. For more information on the preparation steps and mechanical properties, see [5, 15, 16].

All samples were cut into slices of $1 \times 10 \times 10 \text{ mm}^3$, and then mechanically polished with automatic grinding (up to 2500 grit). After grinding with diamond suspensions of 1 μm diameter, they were electro-polished in solution of 2% perchloric acid in 98% ethylene glycol monobutyl ether for about 3 minutes to remove the surface damage introduced by mechanical polishing. The procedure was checked for a similar material by means of depth resolved positron annihilation spectroscopy [17].

Table 1. Chemical composition provided by the suppliers (data in wt.%, balance Fe).

Material	Cr	W	Ti	Si	Ni	Mn	added Y_2O_3
14Cr-non-ODS	13.8	0.98	-	0.27	0.2	0.28	-
14Cr-ODS	13.5	0.9	0.4	0.32	0.17	0.27	0.3
9Cr-ODS*	9.1	1.1	0.3	0.3	0.2	0.3	0.3
ODS-Eurofer**	8.9	1.1	-	0.06	-	0.42	0.3

* 9Cr-ODS-A and 9Cr-ODS-B have the same composition.

** 0.11 wt.% Ta, 0.14 wt.% V.

2.2 Irradiations

The Fe-ion irradiations were performed at the 3 MV-Tandetron accelerator at the Ion Beam Center (IBC) at HZDR, Dresden, Germany. A multi-step approach using different ion energies was applied to achieve an approximately rectangular dpa profile with an average

displacement damage of 10 dpa over a depth of about 1.5 μm . This depth was motivated by the approximate agreement with the extension of the plastic zone of the indentation for an indentation depth of 0.2 μm . The irradiation experiment was designed using the Kinchin-Pease option of the SRIM-2008.4 binary collision code [18] assuming a displacement threshold of 40 eV [19]. The irradiation parameters applied during the three steps are summarized in Table 2 in terms of energy and ion fluence. The calculated cross-section dpa profile of the three-step irradiation is shown in Fig. 1. Irradiation experiments were performed at 300 $^{\circ}\text{C}$ and 500 $^{\circ}\text{C}$. To this end, the samples were fixed on a heating target. The temperature was controlled by means of a thermocouple at the back of the samples. All samples exposed to the same irradiation condition were irradiated in the same irradiation experiment to guarantee comparability. The ion beam was scanned over the whole surface to achieve a homogeneous irradiation.

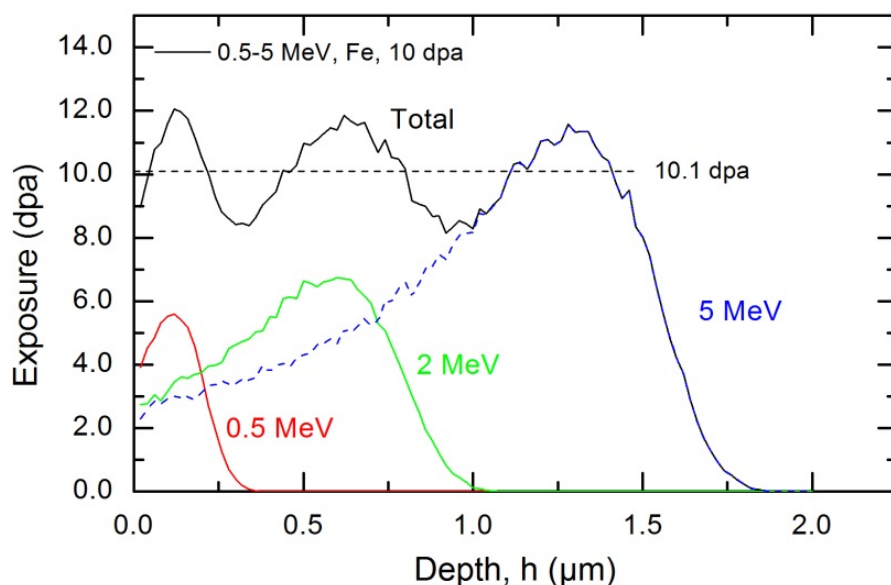


Fig. 1. dpa distribution of the three-step irradiation calculated by SRIM.

Table 2. Parameters of the three-step irradiation.

Step	Ion	Energy (MeV)	Ion fluence ($1/\text{cm}^2$)
1	Fe^+	0.5	3.7×10^{15}
2	Fe^+	2	6.1×10^{15}
3	Fe^{2+}	5	1.15×10^{16}

2.3 Methods

2.3.1 EBSD for unirradiated alloys

The microstructure was characterized and the grain size distribution was measured by EBSD using Zeiss NVision FEG-SEM equipment. For grain size determination, assemblies of about 1000 grains were considered using a fixed minimum misorientation angle of 10° . More information about this equipment can be found in [20].

2.3.2 SANS for unirradiated alloys

SANS experiments were performed at the SANS instrument V4 of Helmholtz-Zentrum Berlin (HZB) using a neutron wavelength of 0.605 nm, a saturation magnetic field of 1.57 Tesla and two sample-detector distances of 1.7 m and 8 m. The data analysis was based on the software package BerSANS [21] and a self-written Monte Carlo code [22] for transforming scattering curves into nanoparticle size distributions. The size distributions were derived from the magnetic scattering cross sections as functions of the scattering vector, Q , after separating nuclear and magnetic scattering and subtracting the background consisting of a part proportional to Q^{-4} and incoherent scattering. In order to calculate the magnetic contrast, the scatterers (i.e. oxide nanoparticles) were assumed to be non-magnetic.

2.3.3 TEM for unirradiated alloys

TEM investigation of unirradiated 9Cr-ODS-A and 9Cr-ODS-B was carried out at CIEMAT Madrid using a JEOL JEM-2010 TEM with LaB_6 filament operating at 200 keV. Thin foils were prepared by mechanical polishing of 3 mm diameter discs up to 0.1 mm. The final thinning up to electron transparency was performed by electro-polishing in a Struers Tenupol-5 device with a reactive mixture of 5% perchloric acid and 95% methanol at $-60\text{ }^\circ\text{C}$. The dislocation analysis was done by image analysis of different grains (diffraction vector $g = (110)$) measuring the total dislocation length, employing JMicroVision software.

2.3.4 Nanoindentation

A Universal Nanomechanical Tester UNAT (ASMEC/Zwick) equipped with a Berkovich indenter was utilized to measure the hardness of the ion irradiated samples and the unirradiated references. Calibrations of the indenter geometry and the instrument stiffness were based on measurements on two reference materials (fused silica, sapphire) with known elastic modulus. Quasi continuous stiffness measurement (QCSM) was applied with the load superimposed with a sinusoidal oscillation for 3 s at discrete loads while the average load is kept constant. This way, the contact stiffness can be calculated at discrete points along the loading curve using the force and displacement amplitude and taking into account the mass and the damping of the measuring head. With this information, the full loading curve can be exploited to calculate the indentation hardness (H_{IT}) as a function of contact depth (h_c). The tests were performed with a maximum load of 50 mN with corresponding contact depth of about 650 to 750 nm. More than 30 indents per sample were performed. Zero point and thermal drift correction were applied to each individual curve. Thereafter, an average curve was calculated and analyzed using the method described by Oliver and Pharr [23]. The hardness value at a reference depth of 200 nm was chosen as the hardness representative of the irradiated layer and to calculate the irradiation-induced hardness change. This takes into account that the deformed zone in alloy is usually 5-10 times deeper than the contact depth [23-26], i.e. at 200 nm contact depth, the full plastically deformed zone is within the irradiated layer. A linear superposition of the initial hardness and the hardness contribution by the irradiation-induced defects is assumed. Moreover, it is assumed that the indentation size effect (ISE) does not significantly change with irradiation.

3. Results

3.1 Characterization of unirradiated materials

14Cr-ODS, 14Cr-non-ODS and 9Cr-ODS-A exhibit a ferritic microstructure. A tempered martensitic microstructure is present in 9Cr-ODS-B and ODS-Eurofer due to a heat treatment involving austenization, quenching and tempering. Inverse pole figure maps of all materials obtained by EBSD are shown in Fig. 2. The normal vector of the EBSD sample surfaces was chosen to be parallel to the extrusion/rolling direction. Grain size (d_g) was determined using a misorientation angle of 10° . A fine grain size distribution was observed in all materials. The average values of grain size are $0.59 \mu\text{m}$ (14Cr-non-ODS), $0.44 \mu\text{m}$ (14Cr-ODS), $1.20 \mu\text{m}$ (9Cr-ODS-A), $0.73 \mu\text{m}$ (9Cr-ODS-B), and $0.73 \mu\text{m}$ (ODS-Eurofer [15]), as summarized in Table 3. 14Cr-non-ODS (Fig. 2(a)) and 14Cr-ODS (Fig. 2(b)) exhibit smaller average grain size compared with 9Cr-ODS and a texture with $\langle 110 \rangle$ direction preferentially oriented parallel to the extrusion direction. The added ODS particles contribute to forming smaller grains in 14Cr-ODS. Compared with 9Cr-ODS-A, which has the coarsest grains, the grains in 9Cr-ODS-B are refined due to the quenching and martensitic transformation. It is well known that the grains of 14Cr-ODS are elongated in the extrusion direction [14]. This is not taken into account in the average grain size determined from EBSD analyses performed for transverse samples. However, it is reasonable to assume that the short dimensions of the grains separated by high-angle boundaries are most relevant for grain boundary hardening as well as sink strength determination. Indeed, the sink strength is related to the inverse of the mean distance a point defect travels in the solid before becoming trapped [9].

The magnetic scattering curves measured for materials 9Cr-ODS-A, 9Cr-ODS-B, 14Cr-ODS and 14Cr-non-ODS are plotted in Fig. 3 together with the corresponding background curves. Results for ODS-Eurofer were reported in [16]. After background subtraction, the size distributions of the oxide nanoparticles were derived for all materials from the magnetic scattering cross sections assuming non-magnetic oxide nanoparticles. The calculated average diameters, number densities and volume fractions of the oxide nanoparticles are summarized in Table 3. The measured A -ratios defined as $A = 1 + M/N$, M and N being integrated magnetic and nuclear scattering intensities, respectively, are between 2.3 and 3.1 for all materials. This indicates the presence of Y-Ti-rich oxides [27] except for 14Cr-non-ODS. Different types of oxide nanoparticles will not be distinguished in the discussion of the sink strength in section 4.3.

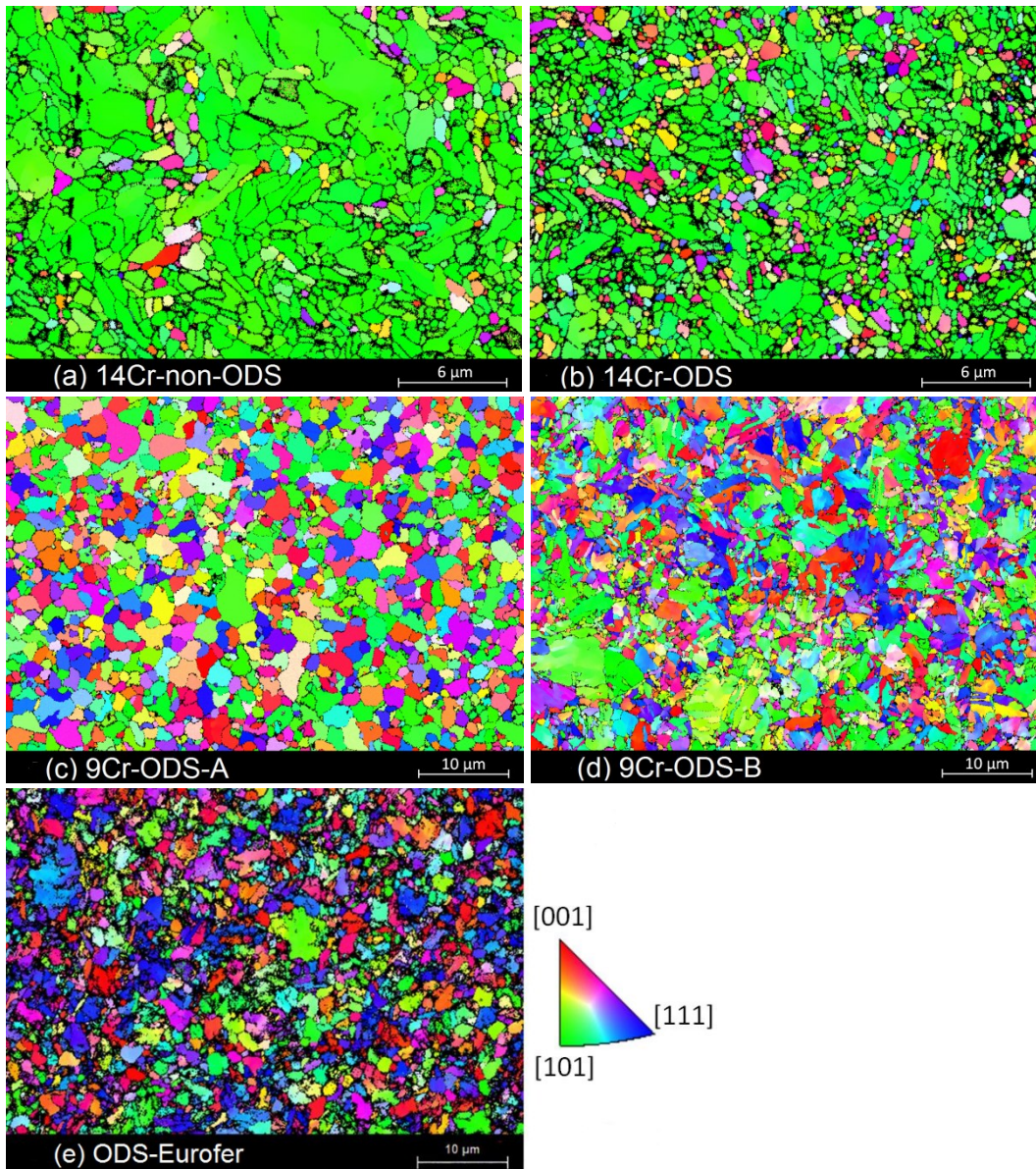


Fig. 2. Inverse pole figure maps obtained by EBSD of 14Cr-non-ODS (a), 14Cr-ODS (b), 9Cr-ODS-A (c), 9Cr-ODS-B (d) and ODS-Eurofer (e) with the normal vector of the sample surface chosen parallel to the extrusion/ rolling direction.

The magnetic scattering curves of the 9Cr and 14Cr ODS alloys of this study are plotted in Figs. 3(a) and (b), respectively, along with the respective background curves. Sharing the same initial manufacturing processes and composition, 9Cr-ODS-A and -B exhibit equal particle distributions, as shown in Fig. 3(a) for the scattering curves. Compared with 9Cr-ODS-A and -B, ODS-Eurofer has slightly larger particles with slightly smaller number density. 14Cr-ODS contains a higher number density of particles than 14Cr-non-ODS, whereas the mean diameters agree (Table 3). It is interesting to note that the number density of nanoparticles is still relatively high in the yttrium-free 14Cr-“non”-ODS alloy. These nanoparticles, which are tentatively interpreted as Cr-rich oxides introduced from oxygen contamination during mechanical alloying, will be taken into account in the discussion. The 14Cr alloys have larger number densities and smaller sizes of particles than each of the 9Cr alloys.

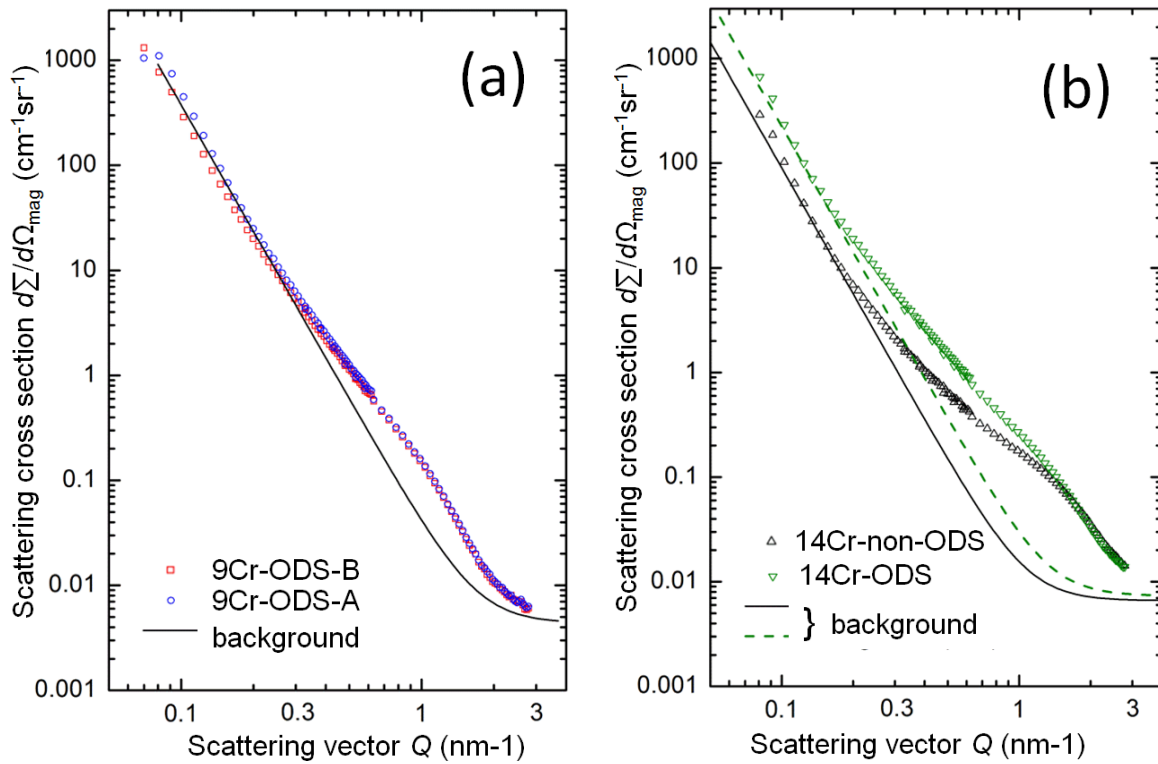


Fig. 3. Measured nuclear scattering cross sections for the unirradiated 9Cr-ODS-A and -B (a), and unirradiated 14Cr alloys (b).

In addition, dislocation densities for all investigated materials were also included. A TEM micrograph is shown in Fig. 4 for 9Cr-ODS-A as an example of dislocation lines. The measured (9Cr-ODS-A and -B) or reported (14Cr-ODS [28] and ODS-Eurofer [29]) dislocation densities are given in Table 3. For 14Cr-non-ODS the same dislocation density as for 14Cr-ODS was assumed.

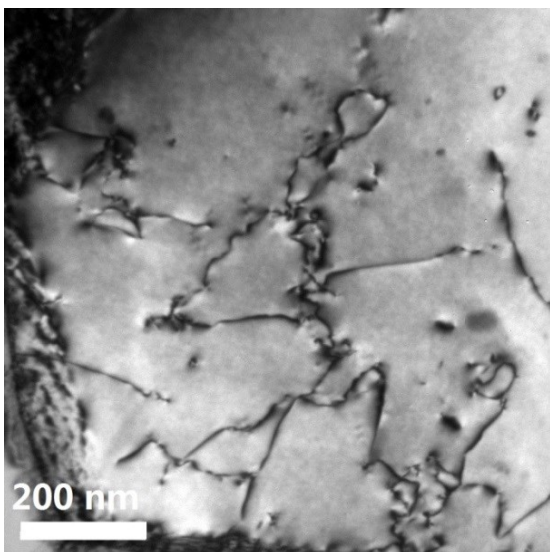


Fig. 4. Bright field image for unirradiated 9Cr-ODS-A

Table 3. Microstructure, indentation hardness and irradiation-induced hardness increase at reference depth of 200 nm.

Material	14Cr- non-ODS	14Cr- ODS	9Cr- ODS-A	9Cr- ODS-B	ODS- Eurofer
Grain size, d_g (μm)	0.59	0.44	1.20	0.73	0.73
Oxide particle diameter, d_p (nm)	2.3	2.3	3.5	3.5	3.8
Oxide particle density, N_p (10^{22} m^{-3})	32.0	44.0	12.3	12.3	11.5
Oxide particle volume fraction, f_p (%)	1.09	1.46	0.51	0.51	0.72
Dislocation density, ρ (10^{14} m^{-2})	5.0	5.0	0.46	3.4	7.0
H_{IT} (GPa)	4.28	4.57	3.55	4.19	4.46
ΔH_{IT} (300 °C) (GPa)	0.58	0.69	1.22	0.96	1.02
ΔH_{IT} (500 °C) (GPa)	0.31	0.26	1.15	0.74	0.61

The grain size and particle distribution are tightly associated with the mechanical properties. Fig. 5(a) shows the indentation hardness measured as a function of contact depth for all unirradiated materials. The individual points represent values averaged over all indentations. The error bars represent the mean error of the average value. Fig. 5(a) shows that 14Cr-ODS exhibits the largest and 9Cr-ODS-A the lowest hardness at all depths. The indentation hardness of the unirradiated materials is taken as reference to calculate the irradiation-induced hardness changes.

3.2 Irradiation response

Figs. 5(b) to (f) represent the indentation hardness as a function of contact depth after Fe-ion irradiation at 300 °C and 500 °C up to 10 dpa and for the unirradiated reference samples. Irradiation-induced hardness increase occurred at both temperatures for all materials, but was more pronounced at 300 °C. All plotted curves for 300 °C display an approximately flat stage and a subsequent gradual reduction. The curves measured after irradiation at 500 °C show lower hardness at low depth. This means that the hardening produced by irradiation was weaker in the near-surface layer. The indentation hardness values taken at the reference depth of 200 nm are graphically summarized in Fig. 6(a) for all unirradiated and irradiated materials. The differences between the hardness of the irradiated and the corresponding unirradiated materials are given in Fig. 6(b).

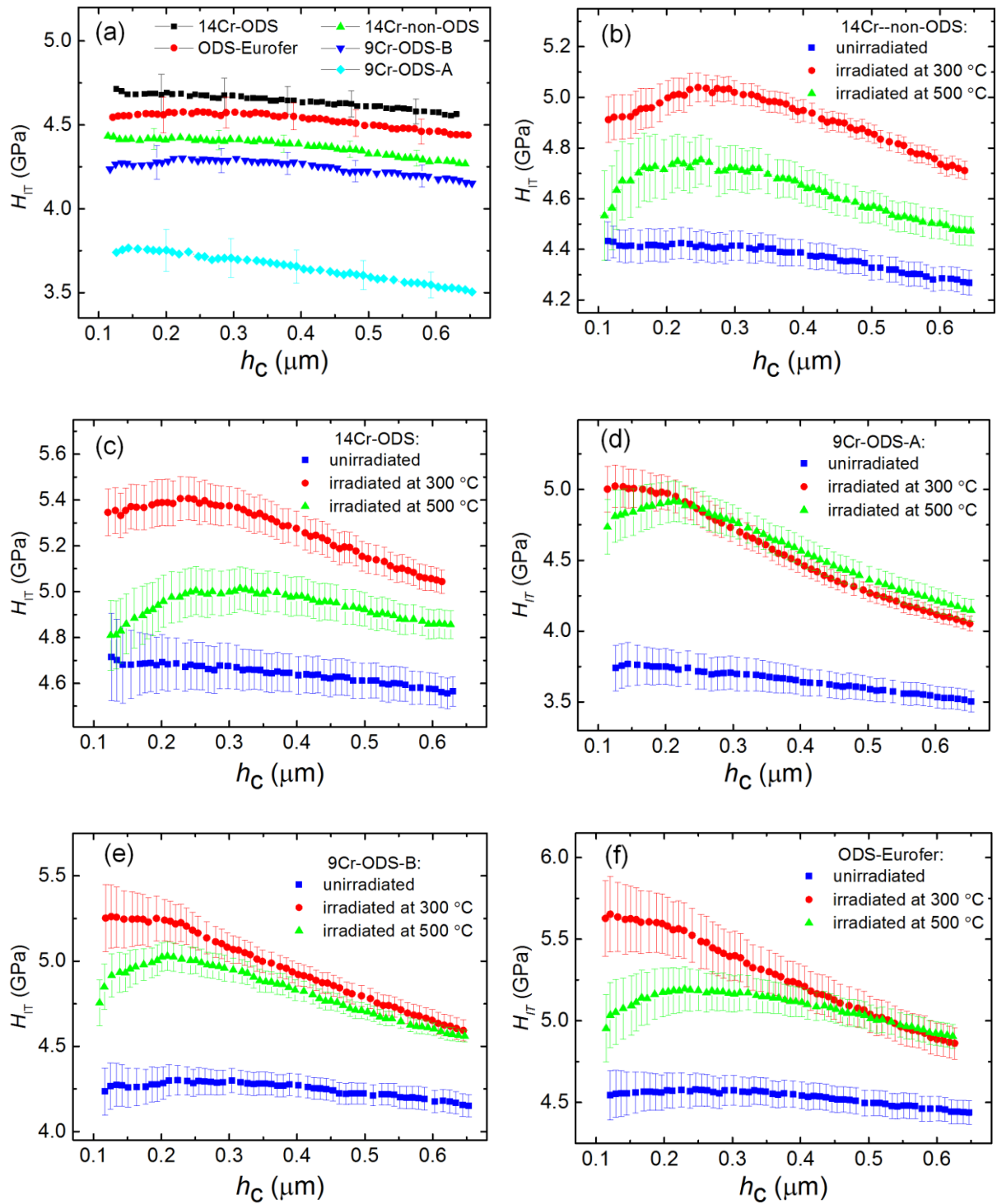


Fig. 5. Nanoindentation hardness as a function of contact depth: (a) comparison of hardness of unirradiated materials, (b) – (f) comparison of hardness change after irradiations at 300 °C and 500 °C.

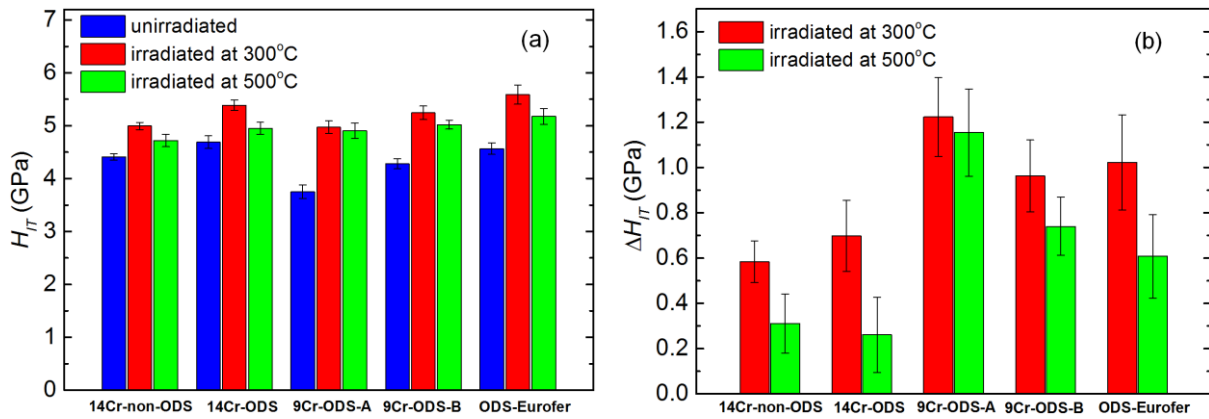


Fig. 6. Representations of hardness value (a) and corresponding hardness increase (b) chosen at a reference depth of 200 nm.

4. Discussion

4.1 Unirradiated materials

The plot of the indentation hardness versus indentation depth, Fig. 5(a), showed that a slight reduction of the indentation hardness with increasing depth was observed for all unirradiated materials at indentation depths larger than 200 nm. The reduction is known as ISE [24, 25]. In addition to the inherent characteristics of materials, sample preparation and test method may affect the level of ISE [25]. In this study, a weak ISE was observed owing to careful sample preparation (see experimental section) and to the hierarchical microstructure covering a similar range of length scales as the indentation size/depth [26].

The observed microstructures and values of the indentation hardness at 200 nm reference depth are summarized in Table 3. It is interesting to compare both microstructures and indentation hardness of the as-received (ferritic) and the quenched and tempered (tempered martensitic) versions of the ODS Fe-9Cr alloy, i.e. 9Cr-ODS-A versus 9Cr-ODS-B. We found that the measured SANS cross sections and, therefore, average size and number density of oxide nanoparticles exactly agree for both conditions indicating stability of the particles during austenitization. The grain size of 9Cr-ODS-B is smaller and the dislocation density is higher than for 9Cr-ODS-A. These two factors explain the higher indentation hardness. The comparison of the data for 9Cr-ODS-B and ODS-Eurofer indicates that the higher indentation hardness of ODS-Eurofer is mainly due to the higher dislocation density

The comparison of the particle characteristics of the non-ODS and ODS versions of the Fe-14Cr alloy indicates that the non-ODS alloy produced via the powder metallurgy route but without addition of yttria surprisingly also contains a high number density of nanoparticles. These are tentatively interpreted as Cr oxides. The higher number density and smaller grain size of the 14Cr-ODS (as compared to 14Cr-non-ODS) results in the higher indentation hardness.

The higher indentation hardness observed for the 14Cr alloys compared with the 9Cr alloys except for ODS-Eurofer is consistent with smaller grain size, higher number density of nanoparticles and higher dislocation density. A prediction of the hardness of the unirradiated

alloys based on a quantitative description of the individual hardening mechanisms is beyond the scope of the paper.

4.2 Impact of irradiation temperature on hardening

Figs. 5(b) to (f) show that a common feature of all materials irradiated at 500 °C is a decrease of indentation hardness at decreasing indentation depth in the near-surface region. This indicates an important role of the sample surface in the evolution of irradiation-induced defects. A possible interpretation is the operation of the surface as defect sink in combination with either point defect diffusion or glide of dislocation loops to the surface. A similar surface effect is well known from TEM observations on samples irradiated as thin foils [30, 31]. Another possible explanation for the decrease of indentation hardness at decreasing indentation depth in the near-surface region is related to the sequence of the three-step irradiations. Indeed, it is possible that a fraction of the irradiation-induced defects introduced during steps 1 and 2 of the irradiation (see Table 2) will recombine during steps 2 and 3, when the whole sample is again exposed to the irradiation temperature. The healing effect on the nanohardness would presumably be more pronounced for the irradiations at 500 °C.

At higher indentation depths, where surface effects do not play a role, two kinds of behavior as a function of irradiation temperature have to be distinguished. For the 9Cr-ODS alloys, we have found equal hardening for both temperatures within experimental error indicating similar distributions of irradiation-induced nanostructures, although a coincidental compensation of different contributions cannot be excluded. In contrast, hardening observed for the 14Cr alloys irradiated at 500 °C was significantly less compared to 300 °C. This difference indicates dissimilar types or distributions of irradiation-induced nanostructures. The counterparts, 300 °C versus 500 °C and 9Cr versus 14Cr, imply a special role of Cr-rich α' -phase particles according to the Fe-Cr phase diagram.

Irradiation-enhanced α' formation was frequently reported in the literature [32-36]. According to the equilibrium Fe-Cr phase diagram [37-39], significant amounts of α' are expected to form in Fe-14Cr alloys at 300 °C, but much less α' can form in Fe-9Cr alloys at 300 °C and no α' can form at 500 °C for both Cr contents. The equilibrium volume fraction of α' as a function of Cr at 300 °C is summarized in Table 4. The formation of these volume fractions of α' gives rise to additional hardening, which can be roughly estimated on the basis of the dispersed-barrier hardening model, Eq. (1):

$$\Delta H_{T,\alpha'} = \frac{\alpha}{\beta} M G b \sqrt{N d} \quad (1)$$

Here, the obstacle strength, α , for α' -phase particles is assumed to be 0.015 according to [40], the conversion factor, β , between yield stress increase and indentation hardness increase is taken to be 0.44 [41], $M = 3$ is the Taylor factor, $G = 84$ GPa is the shear modulus, $b = 0.248$ nm is the Burgers vector, $d = 2$ nm is the mean diameter of α' -phase particle according to [40] and N is the number density of particles estimated from the equilibrium volume fraction assuming a monomodal distribution of spherical α' -phase particles.

Table 4. Calculated equilibrium fraction of α' (vol%) as a function of Cr at 300 °C, hardening caused by α' -phase particles calculated according to Eq. (1) and measured hardening (reference depth 400 nm, taken from Fig. 5) at 300 °C in excess of 500 °C.

Material	14Cr- non-ODS	14Cr- ODS	9Cr- ODS-A	9Cr- ODS-B	ODS- Eurofer
Cr (wt.%)	13.8	13.5	9.1	9.1	8.9
Equilibrium fraction of α' at 300 °C (vol%)	6.8	6.5	1.3	1.3	1.1
$\Delta H_{IT,\alpha'}$ according to Eq.(1) (GPa) *	0.38	0.38	0.17	0.17	0.15
$\Delta H_{IT,300^\circ\text{C}} - \Delta H_{IT,500^\circ\text{C}}$, measured (GPa)	0.3	0.3	<0.03	0.1	0.1

* Solubility limits of Cr in α and Fe in α' are 8 wt.% and 2 wt.%, respectively, according to the Fe-Cr phase diagram reported in [39]. wt.% of α' calculated from lever rule and converted to vol% of α' .

The theoretical hardness increase due to α' -phase particles derived from Eq. (1) and the measured excess hardness at 300 °C (compared to 500 °C) are shown in Table 4. The measured hardness difference was taken at an indentation depth of 400 nm in order to avoid interference with surface effects observed for 500 °C. At this indentation depth, the hardness values are already reduced due to the substrate effect, because the plastic zones of the indentations extend deeper into the bulk than the ion irradiations. The comparison of the estimated hardening due to α' -phase particles and the excess hardness measured at 300 °C shows a trend telling that the higher the equilibrium fraction of α' and the higher the resulting theoretical α' -induced hardening, the more the hardness measured at 300 °C exceeds the hardness measured at 500 °C, a temperature for which α' cannot form.

This is another indication that the initially presumed role of α' -phase particles might indeed be applicable. However, this indication must not be overstressed. It is not clear if the complete amount of equilibrium α' may have formed after ion irradiation up to 10 dpa. In this context, it is important to note that:

- α' formation was indeed observed in Fe-Cr alloys neutron-irradiated at 300 °C up to 0.6 dpa [33, 38]. These α' -phase particles contributed essentially to the hardening for Fe-12%Cr [40].
- Less evidence on α' formation seems to be available for neutron-irradiated ODS steels, see for example [42].
- No α' was recently reported for an Fe-12%Cr alloy ion-irradiated at 300 °C up to 0.5 dpa [43]. This phenomenon was interpreted as a consequence of the injected interstitials [44].

The arguments listed above show that further investigations are needed to clarify the possible contribution of α' -phase particles to the hardening at 300 °C observed in this study. On the other hand, α' -phase formation is strictly excluded at 500 °C. This situation led us to focus on the 500 °C irradiations in section 4.3.

4.3 Impact of the initial microstructure on hardening

The discussion of the irradiation-induced hardness changes shown in Fig. 6(b) is performed on the basis of the microstructural parameters collected in Table 3. Generally speaking, there are two different aspects of irradiation hardening, which can be cast into the following questions:

- (1) How do the glide obstacles of the initial microstructure and the irradiation-induced nanofeatures of different kinds superimpose to substantiate the hardness measured for the irradiated materials? This question was studied for the less complex case of neutron-irradiated Fe-Cr alloys [40]. As compared to [40], SANS is not applicable to the ion-irradiated thin layers of the present case; TEM is in progress within the collaborative project, but it is difficult to quantify the distribution of irradiation-induced nanofeatures such as loops in ion-irradiated technical Fe-based alloys by means of TEM; Atom probe tomography (APT) of the present set of ion-irradiated ODS alloys has not been included in the project, but should be envisaged as complementary study. Thus, it is a future challenge to answer question (1).
- (2) How does the initial microstructure enhance or impede the evolution of the irradiation-induced microstructure and thus give rise to higher or less amounts of irradiation hardening? This question is addressed below within the concept of sink strength. The characteristics of the irradiation-induced nanofeatures (loops, defect-solute clusters) appear as implicit variables, the values of which remain unknown.

Sinks for irradiation-induced point defects play a particular role in the microstructure evolution during irradiation, as they reduce the concentration of point defects available for irradiation-enhanced solute atom diffusion. For the present set of alloys, three types of sinks are potentially operative: dislocations, particle-matrix interfaces, and grain boundaries [1, 4, 9, 45, 46]. The specific sink strengths of dislocations, particles and grain boundaries and the total sink strength, denoted by S_d , S_p , S_g and S_{total} , respectively, can be calculated according to Eqs. (2) to (5) [4, 9, 47, 48].

$$S_{total} = S_d + S_p + S_g \quad (2)$$

$$S_d = Z_d \rho \quad (3)$$

Having checked that capture of defects by dislocations is essentially diffusion-controlled [9] for the present microstructures, a value of 1.2 was estimated for the dislocation capture efficiency Z_d according to the method described in [9]. As we are not interested in swelling here, the capture of vacancies and interstitials was not distinguished.

$$S_p = 2\pi N_p d_p \quad (4)$$

Eq. (4) is applied here as an approximation. It is valid for incoherent particles. We assume that both coherent and incoherent oxide nanoparticles are present in the materials investigated here. Coherent particles differ from incoherent particles with respect to the fact that they operate as point defect traps rather than sinks. Trapped point defects do not lose their identity and may recombine at a later time [9].

$$S_g = 6\sqrt{S_{total}/d_g} \quad (5)$$

Eq. (5) is derived for the case that $(S_{total})^{1/2}d_g \gg 1$ [8, 9]. Note that the sum of Eqs. (3) to (5) constitute an implicit equation for S_{total} . The calculated values of the partial and total sink strengths are summarized in Table 5.

Table 5. Calculated sink strength and indentation hardness increase measured at a reference depth of 200 nm.

Material	14Cr- non-ODS	14Cr- ODS	9Cr- ODS-A	9Cr- ODS-B	ODS- Eurofer
Sink strength of GBs, S_g (10^{14} m^{-2})	7.9	12.3	2.7	4.9	5.3
Sink strength of particles, S_p (10^{14} m^{-2})	46.2	63.6	27.0	27.0	27.5
Sink strength of dislocations, S_d (10^{14} m^{-2})	6.0	6.0	0.6	4.1	8.4
Total sink strength, S_{total} (10^{14} m^{-2})	60.1	81.9	30.3	36.1	41.1
ΔH_{IT} (300 °C) (GPa)	0.58	0.69	1.22	0.96	1.02
ΔH_{IT} (500 °C) (GPa)	0.31	0.26	1.15	0.74	0.61

As the first observation, the 14Cr alloys exhibit smaller hardening than each of the 9Cr alloys for both irradiation temperatures. On the one hand, this observation cannot be due to a possible contribution of α' to hardening (if any), because $\Delta H_{IT,\alpha'}$ is too small and follows the opposite trend (Table 4). On the other hand, the observation is consistent with the larger total sink strengths calculated for the 14Cr alloys. As Table 5 shows, particles contribute most to the total sink strength followed by grain boundaries and dislocations. With the exception of S_d for ODS-Eurofer, the individual contributions are larger for the 14Cr alloys than for the 9Cr alloys.

As the second observation, 9Cr-ODS-B exhibits smaller hardening than 9Cr-ODS-A for both irradiation temperatures. The only difference between these two alloys is related to the heat treatments, which resulted in higher dislocation density and finer grains for 9Cr-ODS-B, but did not change the particle distribution. Therefore, the sink strength of particles S_p cannot be the reason of the smaller hardening of 9Cr-ODS-B. In other words, the smaller grain size and/or the higher dislocation density improve irradiation resistance, although they add only a minor part to the total sink strength.

In the above discussion, we have considered selected groups or pairs of materials in order to evaluate the effect of microstructure parameters. We have found that each of the sink types contributes to the irradiation resistance. A more detailed evaluation of the roles of the individual microstructure parameters is beyond the scope of the present study. However, it is interesting to analyze the irradiation-induced hardening as a function of total sink strength for the whole set of alloys as shown in Fig. 7 for the irradiations at 500 °C. The 300 °C irradiations are placed back because of the unresolved situation for α' -phase particles. In Fig. 7, we have introduced a power-law fit to the experimental data. The overall trend confirms the expectation that higher total sink strength gives rise to less hardening. We do not dispose of an analytical model predicting the amount of irradiation-induced hardening as a function of total sink strength. However, the fit curve represents an inverse relationship, which may serve as a rough empirical approximation for the materials and conditions of this study. Although the 300 °C irradiations are excluded from Fig. 7, it is interesting to note that Table 5 indicates a similar but weaker trend.

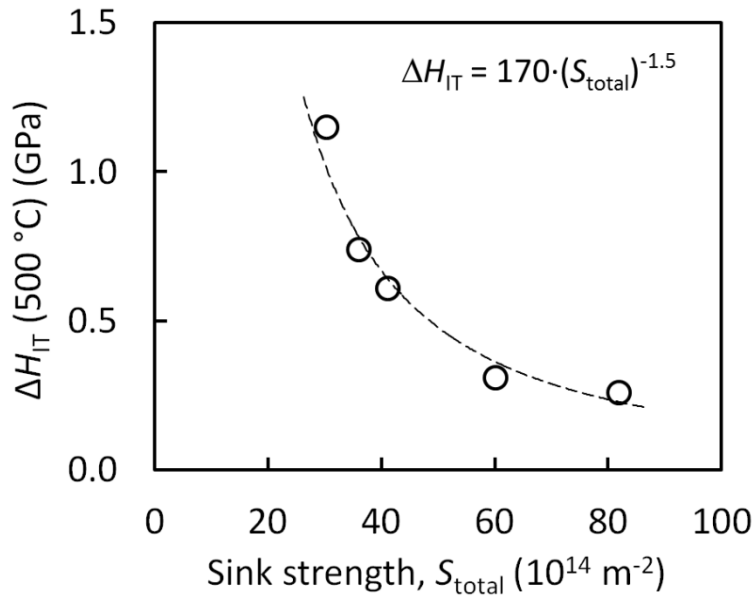


Fig. 7. Irradiation-induced hardness change at 500 °C as a function of total sink strength.

A similar analysis was performed in [4] on the basis of a broader range of sink strengths, namely from 10^{14} m^{-2} to $4 \times 10^{16} \text{ m}^{-2}$. They observed a low-sink-strength domain, where hardening is independent of sink strength, and a high-sink-strength domain, where hardening strongly decreases. The range of sink strength investigated in the present study is close to the transition range between both domains.

5. Conclusions

To investigate the impact of microstructures on self-ion irradiation-induced hardening, three-step irradiations were performed on a set of ODS and non-ODS 9%Cr and 14%Cr alloys at 300 °C and 500 °C. EBSD and SANS were applied to characterize their grain size and particle size distributions, while nanoindentation was used to measure their hardness change after irradiation. Based on the present results and discussion, the following conclusions were drawn:

1. As expected, unirradiated alloys with higher Cr content, smaller grain size, higher dislocation density and higher ODS particle concentration show higher initial hardness.
2. A pronounced decrease of indentation hardness at decreasing indentation depth in the near-surface region was observed for all alloys irradiated at 500 °C. There are two possible interpretations. On the one hand, the surface can act as an efficient planar sink site for irradiation-induced defects. On the other hand, defects introduced during steps 1 and 2 of the three-step irradiation may heal up during subsequent steps, when the whole sample is again exposed to the irradiation temperature.
3. Due to larger total sink strengths, the 14Cr alloys exhibit less hardening than each of the 9Cr alloys for both irradiation temperatures.
4. With the same particle sink strength, 9Cr-ODS-B exhibits smaller hardening than 9Cr-ODS-A for both irradiation temperatures, which suggests smaller grain size and/or higher dislocation density do improve irradiation resistance, although they have minor proportions in the total sink strength.

5. The hardening observed for the present set of alloys irradiated at 500 °C empirically follows an inverse relationship as a function of the total sink strength.

Acknowledgement

This work was supported by the FP7 project MatISSE (Grant Agreement No. 604862). The authors appreciate funding from the China Scholarship Council (CSC). The work contributes to the Joint Programme on Nuclear Materials (JPNM) of the European Energy Research Alliance (EERA). Access to the SANS instrument V4 at HZB Berlin and to the ion irradiation facilities at the Ion Beam Center of HZDR is gratefully acknowledged. Special thanks to Gudrun Müller and Uwe Keiderling for assistance with the EBSD and SANS experiments, respectively. The materials were provided by KIT Karlsruhe, Germany, and CEA Saclay, France.

References

- [1] S. Ukai, M. Fujiwara, Perspective of ODS alloys application in nuclear environments, *Journal of Nuclear Materials* 307–311, Part 1 (2002) 749-757.
- [2] K. Murty, I. Charit, Structural materials for Gen-IV nuclear reactors: Challenges and opportunities, *Journal of Nuclear Materials* 383(1) (2008) 189-195.
- [3] C. Fazio, D.G. Briceno, M. Rieth, A. Gessi, J. Henry, L. Malerba, Innovative materials for Gen IV systems and transmutation facilities: The cross-cutting research project GETMAT, *Nucl Eng Des* 241(9) (2011) 3514-3520.
- [4] S.J. Zinkle, L.L. Snead, Designing Radiation Resistance in Materials for Fusion Energy, *Annu Rev Mater Res* 44 (2014) 241-267.
- [5] R. Lindau, A. Möslang, M. Schirra, P. Schlossmacher, M. Klimenkov, Mechanical and microstructural properties of a hipped RAFM ODS-steel, *Journal of Nuclear Materials* 307–311, Part 1 (2002) 769-772.
- [6] G. Ackland, Controlling Radiation Damage, *Science* 327(5973) (2010) 1587-1588.
- [7] X.M. Bai, A.F. Voter, R.G. Hoagland, M. Nastasi, B.P. Uberuaga, Efficient annealing of radiation damage near grain boundaries via interstitial emission, *Science* 327(5973) (2010) 1631-1634.
- [8] S. Pasebani, I. Charit, J. Burns, S. Alsagabi, D.P. Butt, J.I. Cole, L.M. Price, L. Shao, Microstructural stability of a self-ion irradiated lanthana-bearing nanostructured ferritic steel, *Journal of Nuclear Materials* 462 (2015) 191-204.
- [9] G.S. Was, *Fundamentals of radiation materials science : metals and alloys*, Springer, Berlin ; New York, 2007.
- [10] A. Möslang, C. Adelhelm, R. Heidinger, Innovative materials for energy technology, *International Journal of Materials Research* 99(10) (2008) 1045-1054.
- [11] D.A. McClintock, M.A. Sokolov, D.T. Hoelzer, R.K. Nanstad, Mechanical properties of irradiated ODS-EUROFER and nanocluster strengthened 14YWT, *Journal of Nuclear Materials* 392(2) (2009) 353-359.
- [12] J. Henry, X. Averty, A. Alamo, Tensile and impact properties of 9Cr tempered martensitic steels and ODS-FeCr alloys irradiated in a fast reactor at 325° C up to 78dpa, *Journal of Nuclear Materials* 417(1) (2011) 99-103.
- [13] A. Karch, *Étude des évolutions microstructurales lors de la transformation à chaud d'aciers ferritiques renforcés par dispersion d'oxydes*, Ecole Nationale Supérieure des Mines de Paris, 2014.

- [14] M. Serrano, M. Hernández-Mayoral, A. García-Junceda, Microstructural anisotropy effect on the mechanical properties of a 14Cr ODS steel, *Journal of Nuclear Materials* 428(1-3) (2012) 103-109.
- [15] C. Heintze, F. Bergner, M. Hernández-Mayoral, R. Kögler, G. Müller, A. Ulbricht, Irradiation hardening of Fe–9Cr-based alloys and ODS Eurofer: Effect of helium implantation and iron-ion irradiation at 300 °C including sequence effects, *Journal of Nuclear Materials* 470 (2016) 258-267.
- [16] C. Heintze, F. Bergner, A. Ulbricht, M. Hernández-Mayoral, U. Keiderling, R. Lindau, T. Weissgärber, Microstructure of oxide dispersion strengthened Eurofer and iron–chromium alloys investigated by means of small-angle neutron scattering and transmission electron microscopy, *Journal of Nuclear Materials* 416(1) (2011) 35-39.
- [17] G. Brauer, W. Anwand, W. Skorupa, J. Kuriplach, O. Melikhova, C. Moisson, H. von Wenckstern, H. Schmidt, M. Lorenz, M. Grundmann, Defects in virgin and N⁺-implanted ZnO single crystals studied by positron annihilation, Hall effect, and deep-level transient spectroscopy, *Phys Rev B* 74(4) (2006).
- [18] J.F. Ziegler, J.P. Biersack, M.D. Ziegler, SRIM, the stopping and range of ions in matter, (2008).
- [19] ASTM Standard E521, Standard Practice for Neutron Radiation Damage Simulation by Charged-particle Irradiation, ASTM International, West Conshohochken Philadelphia, PA, 1996.
- [20] I. Hilger, F. Bergner, T. Weißgärber, Bimodal Grain Size Distribution of Nanostructured Ferritic ODS Fe–Cr Alloys, *Journal of the American Ceramic Society* 98(11) (2015) 3576-3581.
- [21] U. Keiderling, The new 'BerSANS-PC' software for reduction and treatment of small angle neutron scattering data, *Applied Physics A: Materials Science & Processing* 74 (2002) s1455-s1457.
- [22] A. Wagner, F. Bergner, R. Chaouadi, H. Hein, M. Hernández-Mayoral, M. Serrano, A. Ulbricht, E. Altstadt, Effect of neutron flux on the characteristics of irradiation-induced nanostructures and hardening in pressure vessel steels, *Acta Materialia* 104 (2016) 131-142.
- [23] W.C. Oliver, G.M. Pharr, An improved technique for determining hardness and elastic modulus using load and displacement sensing indentation experiments, *Journal of Materials Research* 7(06) (1992) 1564-1583.
- [24] W.D. Nix, H. Gao, Indentation size effects in crystalline materials: a law for strain gradient plasticity, *Journal of the Mechanics and Physics of Solids* 46(3) (1998) 411-425.
- [25] S. Bull, On the origins and mechanisms of the indentation size effect, *Zeitschrift für Metallkunde* 94(7) (2003) 787-792.
- [26] X. Hou, N.M. Jennett, M. Parlinska-Wojtan, Exploiting interactions between structure size and indentation size effects to determine the characteristic dimension of nano-structured materials by indentation, *Journal of Physics D: Applied Physics* 46(26) (2013) 265301.
- [27] I. Hilger, F. Bergner, A. Ulbricht, A. Wagner, T. Weißgärber, B. Kieback, C. Heintze, C.D. Dewhurst, Investigation of spark plasma sintered oxide-dispersion strengthened steels by means of small-angle neutron scattering, *Journal of Alloys and Compounds* 685 (2016) 927-935.
- [28] M. Praud, F. Momprou, J. Malaplate, D. Caillard, J. Garnier, A. Steckmeyer, B. Fournier, Study of the deformation mechanisms in a Fe–14% Cr ODS alloy, *Journal of Nuclear Materials* 428(1) (2012) 90-97.

- [29] I. Kuběna, J. Polák, T.P. Plocinski, C. Hébert, V. Škorík, T. Kruml, Microstructural stability of ODS steels in cyclic loading, *Fatigue & Fracture of Engineering Materials & Structures* 38(8) (2015) 936-947.
- [30] Z. Yao, M. Hernández-Mayoral, M. Jenkins, M. Kirk, Heavy-ion irradiations of Fe and Fe–Cr model alloys Part 1: Damage evolution in thin-foils at lower doses, *Philosophical Magazine* 88(21) (2008) 2851-2880.
- [31] M. Hernández-Mayoral, Z. Yao, M. Jenkins, M. Kirk, Heavy-ion irradiations of Fe and Fe–Cr model alloys Part 2: Damage evolution in thin-foils at higher doses, *Philosophical Magazine* 88(21) (2008) 2881-2897.
- [32] M. Mathon, Y. De Carlan, G. Geoffroy, X. Averty, A. Alamo, C. De Novion, A SANS investigation of the irradiation-enhanced $\alpha - \alpha'$ phases separation in 7–12 Cr martensitic steels, *Journal of nuclear materials* 312(2) (2003) 236-248.
- [33] C. Heintze, F. Bergner, A. Ulbricht, H. Eckerlebe, The microstructure of neutron-irradiated Fe–Cr alloys: A small-angle neutron scattering study, *Journal of Nuclear Materials* 409(2) (2011) 106-111.
- [34] V. Kuksenko, C. Pareige, C. Genevois, F. Cuvilly, M. Roussel, P. Pareige, Effect of neutron-irradiation on the microstructure of a Fe–12at.% Cr alloy, *Journal of Nuclear Materials* 415(1) (2011) 61-66.
- [35] V. Kuksenko, C. Pareige, P. Pareige, Cr precipitation in neutron irradiated industrial purity Fe–Cr model alloys, *Journal of Nuclear Materials* 432(1–3) (2013) 160-165.
- [36] M.-H. Mathon, Y. de Carlan, X. Averty, A. Alamo, C. de Novion, Small angle neutron scattering study of irradiated martensitic steels: relation between microstructural evolution and hardening, *Journal of ASTM International* 2(9) (2005) 1-15.
- [37] G. Bonny, D. Terentyev, L. Malerba, On the $\alpha - \alpha'$ miscibility gap of Fe – Cr alloys, *Scripta materialia* 59(11) (2008) 1193-1196.
- [38] F. Bergner, A. Ulbricht, C. Heintze, Estimation of the solubility limit of Cr in Fe at 300 C from small-angle neutron scattering in neutron-irradiated Fe–Cr alloys, *Scripta Materialia* 61(11) (2009) 1060-1063.
- [39] G. Bonny, D. Terentyev, L. Malerba, New contribution to the thermodynamics of Fe-Cr alloys as base for ferritic steels, *Journal of phase equilibria and diffusion* 31(5) (2010) 439-444.
- [40] F. Bergner, C. Pareige, M. Hernández-Mayoral, L. Malerba, C. Heintze, Application of a three-feature dispersed-barrier hardening model to neutron-irradiated Fe–Cr model alloys, *Journal of Nuclear Materials* 448(1–3) (2014) 96-102.
- [41] C. Heintze, F. Bergner, M. Hernández-Mayoral, Ion-irradiation-induced damage in Fe–Cr alloys characterized by nanoindentation, *Journal of Nuclear Materials* 417(1) (2011) 980-983.
- [42] H.J. Jung, D.J. Edwards, R.J. Kurtz, T. Yamamoto, Y. Wu, G.R. Odette, Structural and chemical evolution in neutron irradiated and helium-injected ferritic ODS PM2000 alloy, *Journal of Nuclear Materials* 484 (2017) 68-80.
- [43] C. Pareige, V. Kuksenko, P. Pareige, Behaviour of P, Si, Ni impurities and Cr in self ion irradiated Fe-Cr alloys - Comparison to neutron irradiation, *Journal of Nuclear Materials* 456 (2015) 471-476.
- [44] O. Tissot, C. Pareige, E. Meslin, B. Décamps, J. Henry, Influence of injected interstitials on α' precipitation in Fe – Cr alloys under self-ion irradiation, *Materials Research Letters* (2016) 1-7.
- [45] S. Wurster, R. Pippin, Nanostructured metals under irradiation, *Scripta Materialia* 60(12) (2009) 1083-1087.

- [46] J.P. Wharry, M.J. Swenson, K.H. Yano, A review of the irradiation evolution of dispersed oxide nanoparticles in the b.c.c. Fe-Cr system: Current understanding and future directions, *Journal of Nuclear Materials* 486 (2017) 11-20.
- [47] G. Odette, M. Alinger, B. Wirth, Recent developments in irradiation-resistant steels, *Annu. Rev. Mater. Res.* 38 (2008) 471-503.
- [48] S. Mohan, S. Balaji, S. Amirthapandian, C. David, B. Panigrahi, Effect of heavy ion irradiation at low temperature in Fe-14Cr-0.2 Ti-0.3 Y₂O₃, *Advanced Material Letter* 6(5) (2015) 422-445.